Brain Stimulation 16 (2023) 1557–1565

Contents lists available at ScienceDirect

Brain Stimulation

journal homepage: www.journals.elsevier.com/brain-stimulation

Causal influence of brainstem response to transcutaneous vagus nerve stimulation on cardiovagal outflow

Nicola Toschi [a,b,*], Andrea Duggento [b], Riccardo Barbieri [c], Ronald G. Garcia [a], Harrison P. Fisher [a], Norman W. Kettner [d], Vitaly Napadow [a,d,e], Roberta Sclocco [a,d,e]

[a] Athinoula A. Martinos Center for Biomedical Imaging, Department of Radiology, Massachusetts General Hospital, Harvard Medical School, Charlestown, MA, USA
[b] Department of Biomedicine and Prevention, University of Rome Tor Vergata, Rome., Italy
[c] Department of Electronics, Information, and Bioengineering, Politecnico di Milano, Milan, Italy
[d] Department of Radiology, Logan University, Chesterfield, MO, USA
[e] Scott Schoen and Nancy Adams Discovery Center for Recovery from Chronic Pain, Spaulding Rehabilitation Network, Harvard Medical School, Boston, MA, USA

A B S T R A C T

Background: The autonomic response to transcutaneous auricular vagus nerve stimulation (taVNS) has been linked to the engagement of brainstem circuitry modulating autonomic outflow. However, the physiological mechanisms supporting such efferent vagal responses are not well understood, particularly in humans.
Hypothesis: We present a paradigm for estimating directional brain-heart interactions in response to taVNS. We propose that our approach is able to identify causal links between the activity of brainstem nuclei involved in autonomic control and cardiovagal outflow.
Methods: We adopt an approach based on a recent reformulation of Granger causality that includes permutation-based, nonparametric statistics. The method is applied to ultrahigh field (7T) functional magnetic resonance imaging (fMRI) data collected on healthy subjects during taVNS.
Results: Our framework identified taVNS-evoked functional brainstem responses with superior sensitivity compared to prior conventional approaches, confirming causal links between taVNS stimulation and fMRI response in the nucleus tractus solitarii (NTS). Furthermore, our causal approach elucidated potential mechanisms by which information is relayed between brainstem nuclei and cardiovagal, i.e., high-frequency heart rate variability, in response to taVNS. Our findings revealed that key brainstem nuclei, known from animal models to be involved in cardiovascular control, exert a causal influence on taVNS-induced cardiovagal outflow in humans.
Conclusion: Our causal approach allowed us to noninvasively evaluate directional interactions between fMRI BOLD signals from brainstem nuclei and cardiovagal outflow.

1. Introduction

Cardiovagal control in the brainstem includes both efferent and afferent feedback loops and involves the nucleus tractus solitarii (NTS), found in the dorsal medulla, as the primary target for vagal afference. The largest single projection from the NTS is to the parabrachial nucleus (PBN), located in the pons [1,2]. Additionally, the NTS sends a major projection to the periaqueductal gray matter (PAG) [3]. Rodent models have also shown that ascending projections from the NTS transfer information to monoamine neurotransmitter source nuclei such as the locus coeruleus (LC, noradrenergic) and raphe (serotonergic) nuclei in the pons and midbrain [4–7]. While this subnetwork of brainstem nuclei may represent a complex system of feedback loops that exert control over autonomic functions, the physiological mechanisms supporting enhanced efferent vagal outflow are not yet well understood, particularly in humans.

The noninvasive identification of brainstem nuclei implicated in central autonomic network (CAN) functioning in humans has been notoriously difficult, partly due to the limited sensitivity and intrinsically high influence of physiological noise for detecting functional magnetic resonance imaging (fMRI) signals from small cross-sectional areas of several nuclei using standard methods. However, recent advances have been made in applications of ultrahigh field (e.g., 7T) fMRI to identify brainstem nuclei activity [8–11] and functional connectivity [12–14]. A growing number of studies have now reported brainstem fMRI findings [15–21], despite the difficulties in precisely localizing brainstem fMRI responses. Linking autonomic outflow with brainstem fMRI signals is also challenging. For instance, while cardiovagal tone, an autonomic metric, is classically estimated through static spectral analysis of RR interval time series, a joint analysis with human functional

* Corresponding author. Athinoula A. Martinos Center for Biomedical Imaging, Department of Radiology, Massachusetts General Hospital, Harvard Medical School 149 13th St, Charlestown, MA, 02129, USA.
E-mail address: nicola@nmr.mgh.harvard.edu (N. Toschi).

https://doi.org/10.1016/j.brs.2023.10.007
Received 18 April 2023; Received in revised form 6 October 2023; Accepted 9 October 2023
Available online 11 October 2023

MRI data optimally requires a dynamic, noninvasive strategy to estimate autonomic nervous system activity. To this end, in our previous work, we employed point-process modeling of heat rate variability (HRV) [22] to derive time-resolved cardiovagal tone estimates and successively linked them with brain activity (as measured through functional fMRI). This has allowed the identification of brain regions compatible with central autonomic processing in task-evoked arousal [23], in the resting state [24], and in application to neurological disease [25]. However, these prior studies evaluated the zero-lag correlation between HRV and fMRI time series and did not strictly assess a causal influence between fMRI and cardiovagal outflow metrics.

Moreover, both fMRI and cardiovagal signals are robustly modulated by neuromodulatory interventions. For instance, transcutaneous vagus nerve stimulation (tVNS) approaches targeting the auricular branch of the vagus nerve elicit brainstem activation and HRV responses, with clinical applications for multiple disorders, producing antinociceptive effects in pelvic pain [26] and modulating the trigeminal sensory brain circuitry in migraine [19]. Thus, transcutaneous auricular vagus nerve stimulation (taVNS) can be used to better specify the interplay between brainstem activity and the HRV response, as taVNS is known to drive both physiological responses, particularly when coupled with respiratory gating [27,28]. Respiratory gating refers to the synchronization of an intervention, such as neurostimulation, with specific phases of the respiratory cycle. This synchronization can enhance the efficacy of the intervention by leveraging the natural physiological rhythms of the body. In the context of vagus nerve stimulation, respiratory gating can optimize the delivery of stimuli, potentially enhancing therapeutic outcomes and providing a more targeted approach to modulating neural activity. Specifically, taVNS activates several brainstem nuclei, including the NTS and, by ascending projections, the locus coeruleus (LC), parabrachial nuclei (PBN), periaqueductal gray (PAG), and pontine raphe nuclei [29]. Furthermore, NTS activity is known to be modulated by respiration, receiving inhibitory influence during inhalation and facilitatory influence during exhalation [30–32]. Indeed, we have previously shown that the fMRI response to taVNS in the aforementioned brainstem circuitry is augmented when taVNS is delivered during exhalation [19,26,28]. The response is also modulated by stimulation frequency [27]. However, no study has been able to noninvasively disentangle the directional flow of information between brainstem nuclei and cardiovagal outflow in humans. Understanding directional brain-heart interactions is pivotal because it elucidates the intricate interplay between cerebral processes and cardiac function. This knowledge not only deepens our understanding of physiological homeostasis but also paves the way for novel therapeutic interventions targeting cardiovascular diseases and conditions influenced by brain-heart dynamics.

We present a paradigm for estimating directional brain-heart interactions based on a recent reformulation for Granger causality that includes permutation-based, nonparametric statistics. We employ respiratory-gated taVNS as an intervention and demonstrate that our framework can detect taVNS-evoked functional brainstem nuclei responses with superior sensitivity compared to prior conventional approaches. Furthermore, we employed our causal approach to elucidate the mechanisms by which information is relayed between brainstem nuclei and the cardiovagal response, as driven by taVNS.

2. Methods

2.1. Subjects

We enrolled sixteen (16) healthy adults (9 female, age: 27.0 ± 6.6 years, mean ± SD). All participants provided written informed consent, and all study procedures were approved by the Massachusetts General Brigham Institutional Review Board. Subjects were recruited from the general population of the greater Boston area. All participants underwent a preliminary screening to ensure they fit the inclusion criteria, which included no history of neurological or psychiatric disorders, no history of cardiovascular disorders, and no MRI contraindications. The results for the fMRI response to taVNS stimulation using these data and a more conventional analysis approach have been previously reported [28].

Prior to imaging, participants underwent a behavioral session aimed at familiarizing them with both the stimulation and calibration procedure. The stimulation employed in this study was electrical in nature. TaVNS involves the delivery of electrical impulses through custom MRI-compatible electrodes placed in the cymba conchae of the ear. Participants were instructed to rate stimulation intensity (current amplitude, mA) using a 0 to 10 numerical rating scale, where 0 corresponded to "no sensation" and 10 corresponded to "pain sensory threshold". All subjects were given the goal of a "moderately strong, but not painful sensation", i.e., a subjective, percept-matched score of 4–5/10. While participants were informed that stimulation would be intermittent, they were not told that the stimulation would be gated by the respiration signal. Qualitative debriefing confirmed this lack of awareness.

2.2. Experimental protocol

Every participant underwent separate 8-min fMRI scans. For these scan runs, respiratory-gated auricular vagal afferent nerve stimulation (RAVANS) taVNS stimulation was gated either to the exhalation or inhalation phase of the respiratory cycle (eRAVANS, iRAVANS, respectively). The order of the two stimulation runs was counterbalanced across subjects, and the stimulus intensity was percept-matched to target a 4–5 score based on the calibration procedure described above, which was repeated before every fMRI scan run.

2.3. Stimulation and respiratory gating

For RAVANS taVNS, we employed custom-built, ergonomically shaped electrodes that were MR-compatible by design (Bionik Medical Devices, Bucaramanga, Colombia) and placed within the left cymba conchae (Fig. 1). Stimuli were provided by a current-constant Model S88x stimulator with a stimulus isolation unit (Grass Instruments, Astro-Med, Inc., West Warwick, RI, USA) and provided as biphasic rectangular pulse trains (pulse width = 450 μs, duration: 1 s, stimulus frequency = 25 Hz). During stimulation, respiration was measured through a pneumatic belt placed around the subjects' lower thorax and connected to a pressure transducer (PX138-0.3D5V, Omegadyne, Inc., Sunbury, OH, USA) as described in Ref. [28]. The pressure signal was thus transduced into a voltage that was acquired through a DAQ (National Instruments

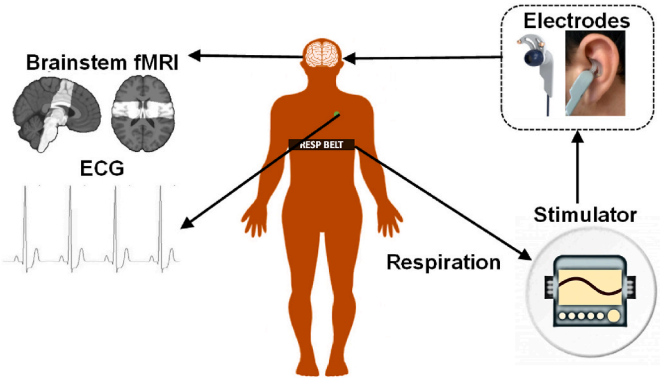

Fig. 1. Experimental setup: partial brain coverage focused on the brainstem and consistent across participants was employed for fMRI. Electrocardiography (ECG) and respiration signals were acquired concurrently with imaging. The respiration signal was employed to gate left auricular stimulation, i.e., respiratory-gated auricular vagal afferent nerve stimulation (RAVANS). Stimulation was delivered through custom MRI-compatible electrodes placed in the cymba conchae of the ear.

USB DAQCard 6009, 14-bit i/o) with LabView 7.0 data acquisition software. End-exhalation and end-inhalation were detected in real-time through in-house developed LabView© code and used to control a miniature high-frequency relay (G6Z-1P-DC5, Omron Electronics Components, Shaumburg, IL, USA), which controlled the onset/offset of stimulation. The end-inhalation timestamp and the stimulus onset for exhalation-gated stimulation were separated by a 0.8 s delay to ensure that the stimulus would be delivered during the exhalation phase. Correspondingly, since the inhalation phase is shorter than the exhalation phase, a delay of 0.1 s was applied between the end-exhalation timestamp and stimulus onset for iRAVANS.

2.4. MRI acquisition and physiological data recording

Blood oxygenation level-dependent (BOLD) fMRI data were collected using a Siemens 7 T whole-body scanner (Siemens Healthineers, Erlangen, Germany) and a custom-built 32-channel receive array and birdcage transmit coil. We employed gradient-echo (GRE) single-shot echo-planar imaging (EPI) to acquire 500 vol per run using a simultaneous multislice acquisition with a multiband factor of 2 and the following parameters: 1.2 mm isotropic voxel size (field of view = 192 × 192 mm^2), 38 coronal slices centered on the brainstem and tilted parallel to the dorsal border of the brainstem using a mid-sagittal localizer, repetition time (TR) = 0.99 s, echo time (TE) = 23 ms, flip angle = 58°, band width = 1562 Hz pix^{-1}, echo spacing = 0.76 ms, using R = 4 in-plane (generalized autocalibrating partially parallel acquisitions (GRAPPA)) acceleration and a robust autocalibration scan [33]. For each functional run, a volume with the opposite phase encoding direction was acquired to facilitate subsequent distortion correction. Additionally, to support coregistration and localization, we also acquired an anatomical reference during the same pulse sequence. This T2*-volume was modified to provide whole-brain coverage while retaining both orientation and shimming volume (126 coronal slices, TR = 3.29 s) of the partial-brain coverage, brainstem–focused data. The T2*-weighted anatomical dataset also contained a volume acquired with the opposite phase encoding direction for the purpose of distortion correction. Finally, electrocardiogram (ECG) and respiration signals were continuously collected simultaneously with MRI scanning (see above) at 500 Hz using an MRI-compatible, noninvasive BIOPAC MP150 system (BIOPAC Systems, Goleta, CA) and a laptop equipped with AcqKnowledge acquisition software (BIOPAC Systems).

2.5. MRI data preprocessing and brainstem mask generation

Preprocessing for fMRI data was performed as described in Ref. [28]. Briefly, this entailed employing a combination of FSL [34](v. 5.0.7), AFNI [35] and in-house created bash scripts to 1) correct fMRI data for cardiorespiratory noise (RETROICOR), slice timing (while accounting for the acquisition order derived from the Simultaneous Multi-Slice strategy), susceptibility-induced distortion (topup, FSL), and head motion (MCFLIRT, FSL). The whole-brain variant T2*-weighted anatomical reference was coregistered to a T2-weighted MNI template (ICBM 2009a Nonlinear Asymmetric template [36]) using concatenated linear and nonlinear transformations (estimated using FSL FLIRT and FNIRT, respectively). The combination of high tissue contrast provided by 7T imaging and high spatial resolution (1.2 mm isotropic) of our datasets allowed us to forego the intermediate functional-to-anatomical (typically T1-weighted) registration step, which is classically employed to warp fMRI volumes into MNI template space, hence reducing the risk of possible coregistration errors driven by differences in susceptibility-induced distortion across modalities. Finally, we transformed a brainstem mask, which was defined in MNI space by thresholding gray and white matter tissue maps at a tissue probability of 0.9, into single-subject native space by inverting the concatenated transformations estimated above (Fig. 2). Since brainstem functional imaging is known to be strongly affected by physiological noise, this mask was used as a boundary to retain the parenchymal signal and exclude brainstem surface vessels and surrounding cerebrospinal fluid that contribute pulsatile noise to voxels within the brainstem. Subsequent causality estimation and groupwise statistical analysis considered voxels within this mask, hence reducing possible smoothing-related contamination within parenchymal voxels. Following masking, minimal smoothing (FWHM = 2 mm) was applied to the BOLD fMRI data to account for some variability in the location of discrete nuclei between subjects.

2.6. High-resolution anatomical underlay

As in our previous papers [27,28], anatomically resolved causality results were visualized over an ex vivo, high-resolution (0.2 mm isotropic) brainstem image consisting of a b0 image from a diffusion–weighted dataset generously provided by the laboratory of Dr. Alan Johnson [37]. This ex vivo brainstem volume was coregistered to MNI space through the Advanced Normalization Tools (ANTs) Toolbox [38] and 3D Slicer (www.slicer.org). Briefly, this entailed initializing the transformation chain using manual landmark-based affine registration [39], generating a brainstem mask on a 0.5 mm resolution MNI152 T1 template in Slicer3D and dilation of this mask to include high-contrast boundaries. Finally, a generic affine registration followed by nonlinear deformation based on the SyN algorithm was performed using mutual information as a similarity metric. The estimated concatenated warps were then used to transform fMRI group-level maps from MNI space to the high-resolution brainstem space for visualization.

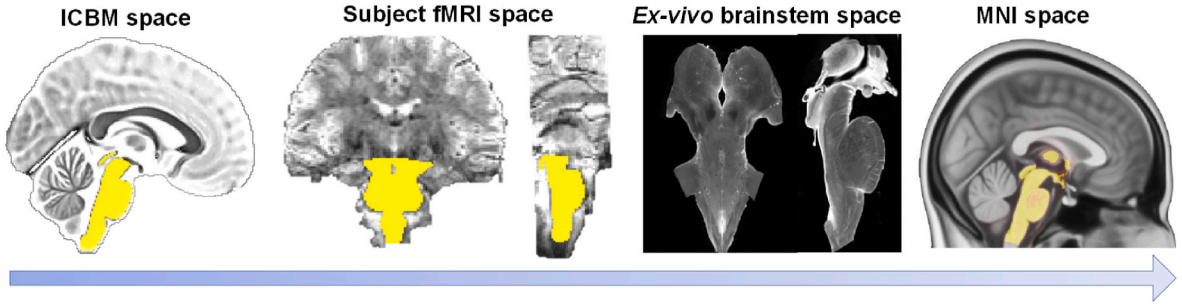

Fig. 2. –A brainstem mask defined in ICBM space was transformed to subjects' individual fMRI space and used to retain brainstem voxels, mitigating physiological noise contamination from surface vessels and CSF that may have been introduced by partial volume effects or spatial smoothing. A high-resolution (0.2 mm isotropic voxels) ex vivo brainstem volume (courtesy of) was transformed to MNI space; inverse warps were then applied to the statistical fMRI maps to visualize clusters over this high-resolution anatomical volume to aid localization and comparison with brainstem atlases.

2.7. Cardiovagal response analysis using instantaneous HF-HRV

To derive an instantaneous estimate of cardiovagal activity concurrent with MRI acquisition, ECG signals were annotated to identify the R-wave peak using an automated in-house algorithm followed by manual inspection, hence generating acquisition-specific RR interval series. In accordance with previous studies, we then employed an instantaneous, physiologically inspired point-process model for heartbeat generation to derive instantaneous estimates for the probability of occurrence of the next R-wave beat [22]. This entails modeling RR interval series through an inverse Gaussian probability function, with the first moment of this probability function modeled using a linear autoregressive model of order k, chosen according to the Schwartz Information Criterion, which represents the information from the k previous beats contained in each RR interval. These autoregressive coefficients then allow for the estimation of spectral measures of heart rate variability (HRV) at arbitrary frequencies. We then derived the time-dependent power within the high-frequency (HF-HRV, 0.15–0.40 Hz) range [40], which, as previously described [23,41,42], is a reliable proxy for parasympathetic (cardiovagal) modulation. HF-HRV time series were sampled in accordance with each TR from the fMRI dataset and convolved with a double-gamma hemodynamic response function (HRF) [43] to allow subsequent joint processing of fMRI and cardiac data. Such analyses would not be possible if using standard, nontime-varying frequency space HRV index estimation.

2.8. Causal analysis strategy

Our fMRI analysis approach included the assessment of causal, i.e., directional relationships between a) the event-related taVNS stimulus design and the voxelwise time-resolved BOLD fMRI signal and b) the voxelwise time-resolved BOLD fMRI signal and the HF-HRV time series. Thus, analysis a) mimics classical first-level general linear model (GLM) analyses in terms of exploring the association between the event-related design and the fMRI response (as in) to assess brainstem response to taVNS stimulation. However, our causal analysis evaluates a putatively directed, possibly delayed, influence of stimulus events on the BOLD fMRI signal, rather than the typically bidirectional instantaneous association between these two time series, as is the case with traditional GLM analysis. Furthermore, analysis b) above evaluated a causal, directed association between brainstem fMRI data and concomitant time-resolved HF-HRV modulation (i.e., causal influence of specific brainstem regions/voxels on cardiovagal modulation, an efferent, peripheral outflow parameter). Our approach employed a recent reformulation of an estimator of between time-series causality that is based on a state-space formulation [44]. Details of this approach appear below.

2.9. Granger causality and its state space formulation in fMRI

In its original formulation, GC is based on the idea of quantifying directed information flow between signals [45]. Most applications of GC in neuroscience thus far have focused on brain connectivity, i.e., inferring directional neural associations between different brain regions from indirect measures such as electroencephalography (EEG), magnetoencephalography (MEG) or fMRI [46,47]. These approaches are often classified into functional connectivity (FC), directed functional connectivity (dFC) and effective connectivity (EC); please see Ref. [48] for a comprehensive overview of these concepts. In the context of fMRI, GC mapping (GCM) has been widely employed to evaluate the existence and directionality of mutual influence between physiological signals and is based on the idea of temporal precedence of information. More specifically, a time series Y is said to G-cause another time series X ($Y \rightarrow X$) when information about the past of Y significantly improves the prediction of the future of X as opposed to employing the past of X alone. In addition, in the context of multivariate systems (i.e., multinode networks), indirect paths within the network may result in the inference of spurious links between X and Y. This is remedied by the formulation of "conditioned" GC. As an example, consider, e.g., three time series X, Y and Z (Fig. 3), which influence each other in some way. The "true" influence of Y on X (i.e., net of any putative effects mediated by Z) would be called the GC of Y on X conditioned on Z. More formally, Y is said to G-cause X conditioned on Z ($Y \rightarrow X|Z$) when information about the past of Y significantly improves the prediction of the future of X as opposed to jointly employing the past of X *and* the past of Z for the same prediction. In the context of fMRI analysis, conditioned GC can be seen as a natural way to extend the idea of "confidence" analysis with multiple explanatory variables (EVs).

Fig. 3 – Conditioned causality (3-variable case, for explanatory purposes only). In this three-variable system, Y is only directly influencing X through path a. However, the dynamics of Y may also be relayed into X although the combined path B + C, which also involves variable Z. A correlation/GLM analysis will not be able to disentangle the first from the second path and would yield a single association measure influenced by both mechanisms. In contrast, conditioned GC ($Y \rightarrow X|Z$) will disentangle the direction and strength of the coupling due to path a only. Note that, typically, multiple paths and feedback loops coexist in the same system.

Over the years, the application of GC to brain networks that generate fMRI time series has been the object of intense debate. One important point has been the effect of local, whole-brain variations in HRF, which, should they affect time-to peak and not only amplitude, would result in a location-dependent temporal shift that may bias GC estimation. This issue was addressed in a study that reinforced that, provided that sampling rates are sufficiently high, the causal influences on the BOLD fMRI signal are invariant to the HRF shape [49]. Moreover, a detailed neural and neurovascular coupling study [50] based on balloon models [51] coupled with structural neuronal models [52,53] demonstrated that GC is able to retain high positive predictive value even in complex networks of simulated BOLD signals. In addition, other investigators have focused

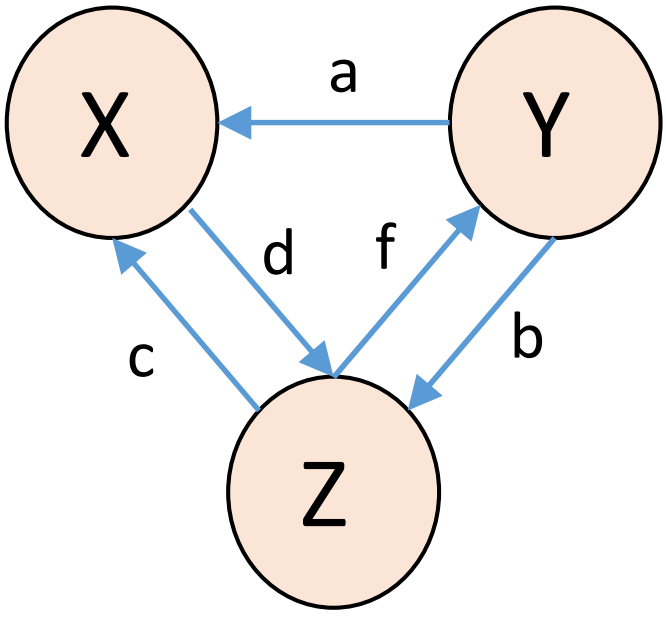

Fig. 3. Conditioned causality (3-variable case, for explanatory purposes only). In this three-variable system, Y is only directly influencing X through path a. However, the dynamics of Y may also be relayed into X although the combined path B + C, which also involves variable Z. A correlation/GLM analysis will not be able to disentangle the first from the second path and would yield a single association measure influenced by both mechanisms. In contrast, conditioned GC ($Y \rightarrow X|Z$) will disentangle the direction and strength of the coupling due to path a only. Note that, typically, multiple paths and feedback loops coexist in the same system.

on typical fMRI parameters such as TR, SNR and neuronal delay, supporting the notion that GC can be applicable for fMRI data analysis [54, 55].

In its most recent state-space formulation (SS-GC), following [56], GC can be operationalized as follows: considering two discrete-time, real-valued vectors $z_t = [x_t, y_t]$, the state space is a formulation in which relationships between a set of input and output variables are described through state variables. For example, a general constant parameter SS model can be described as:

$$\xi_{t+1} = T\xi_t + \omega_t \quad (1)$$

$$z_t = C\xi_t + v_t \quad (2)$$

where equation (1) is the so-called state transition equation and equation (2) is the so-called observation equation. ξ is an unobserved n-dimensional state variable, and ω_t and v_t are zero-mean, white noise processes. The terms "T" and "C" represent the state transition matrix and the observation matrix, respectively. Concretely, matrix C contains the coefficients that map the state variables to the observed data. The variable w_t is formed by the concatenation of x_t, y_t and z_t. Here, y_t and x_t represent the observed time series data, i.e., two different observed time series that we are testing for causal relationships. The term e'_t represents the residuals or the prediction error. Through Kalman filter theory, the state transition and observation equations can be reformulated as follows:

$$\xi_{t+1} = T\xi_t + K_t e_t \quad (3)$$

$$w_t = C\xi_t + e_t \quad (4)$$

where $\xi_t \equiv E[\xi_t \vee w_{t-1}]$, K is the Kalman gain, and $e_t \equiv w_t - E[w_t \vee w_{t-1}]$ constitutes another white noise process (full details can be found in Ref. [44]). In this case, the GC "strength" from Y to X conditioned to Z (Y → X|Z) can be estimated as

$$F_{Y\to X\vee Z} = ln\frac{|\Sigma'_{11}|}{|\Sigma_{11}|} \quad (5)$$

where $\Sigma = cov[e_t e_t^T]$ and $\Sigma' = cov[e'_t e'^T_t]$ refer to a system where all three variables X, Y, and Z are modeled (the so-called full system) and a system where only X and Y are modeled (the so-called partial system), respectively. This framework can be extended to n-dimensional systems (e.g., brain functional connectivity studies) or employed in its bivariate form.

2.10. Joint causal fMRI-HRV data analysis

As mentioned above, two sets of analyses were performed. In the first set of analyses, we aimed to establish how much the event-related taVNS stimulus design causally modulated the BOLD fMRI response. In the second set of analyses, we aimed to establish the directed influence of the brainstem BOLD fMRI signal on instantaneous HF-HRV. For each fMRI scan run, first-level causality analyses were carried out with a conceptually similar approach to "classical" first-level event-related design GLM analysis. Specifically, we estimated the voxelwise stimulus→BOLD SS-GC signal within the brainstem for each subject, hence generating a subjectwise causality strength map. To further reduce cardiac-derived noise contamination of the brainstem fMRI signal, we convolved the time-resolved heart rate (HR) signal derived from the point-process analysis (see above) with a previously reported cardiac response function [57] and included this noise signal in the state space model as a conditioning variable. Hence, we effectively estimated the conditioned SS-GC as follows: Stimulus →(BOLD Signal | Convolved HR).

For the second set of analyses described above, in accordance with our previous work on causal brain-heart interactions, the same strategy was followed. For this analysis, the following voxelwise conditioned SS-GC was performed for each fMRI scan run: BOLD fMRI Signal→ (Convolved HF-HRV | Convolved HR). All first-level analyses were run in native (subject-specific) space and within the transformed brain-stem mask. The resulting voxelwise causality strength maps were transformed into common reference space (ICBM 2009a Nonlinear Asymmetric template) by applying the nonlinear transformations estimated above and were then concatenated for subsequent group-level analyses.

Group-level analysis was executed through a fully nonparametric, permutation-based approach (Fig. 4).

In detail, for both sets of analyses, we tested the null hypothesis of zero groupwise median voxelwise causality strength. This was done by constructing the voxelwise null distribution of this specific hypothesis in a data-driven manner. Specifically, each causality strength was computed for signal pairs (i.e., stimulus and BOLD fMRI time series; BOLD fMRI and HF-HRV time series) where each signal came from different subjects and therefore by definition would not share causal information flow (n.b. each subject's stimulus time series was unique, as it was driven by each individual's respiration patterns). This assumes exchangeability, i.e., that no interaction took place between subjects. This procedure was performed for each possible combination of time series pairs and each voxel within the brainstem mask, hence generating a voxel specific, nonparametric distribution for the null hypothesis of zero groupwise median causality strength. Following this null-distribution definition, the "true" voxelwise distribution (i.e., stemming from pairs of signals collected from the same subject) was estimated in a similar manner. Finally, the medians of these two distributions were compared for each voxel through nonparametric, statistical location testing, hence generating voxelwise p value maps for each tested hypothesis. Due to the limited signal-to-noise ratio (SNR) typical for brainstem responses, significance across the whole brainstem

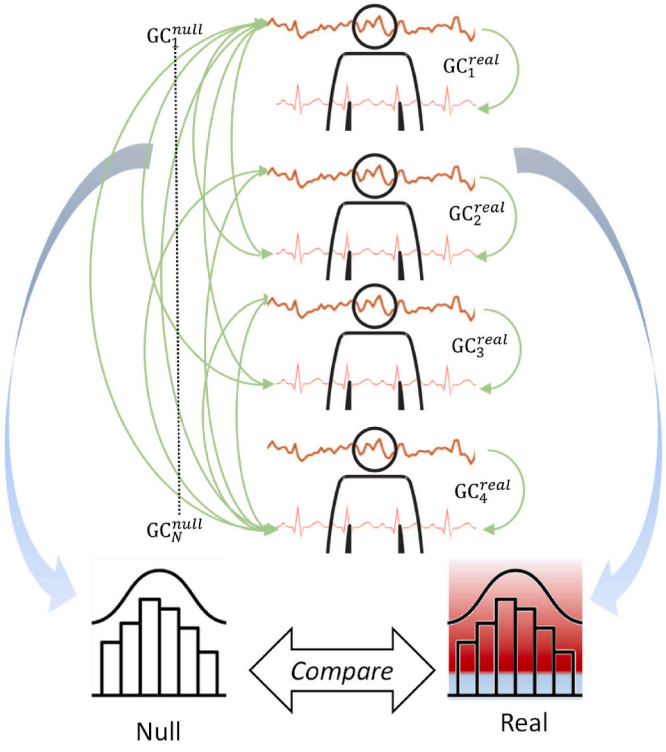

Fig. 4. Outline of second level statistical analysis strategy. "Real" (i.e., within the same subject) SS-GC estimates are generated for each subject, hence giving rise to our data distribution to be tested against the null hypothesis that the median is zero. The null distribution against which to test this hypothesis is generated by calculating "fake" (i.e., combining different subjects in all possible permutations) SS-GC estimates which, by design, should be analytically zero. The median of the two distributions are then compared through a non parametric location test for all voxels within the brainstem mask.

was set at uncorrected $p < 0.001$.

3. Results

No adverse events were recorded, and all subjects completed all experimental sessions without reporting adverse effects. Stimulation characteristics across different conditions showed no significant differences for stimulation current (F score = 0.45, p value = 0.64) or ratings of intensity (F score = 0.06, p value = 0.56) (**Table 1**). In,Table 1 eRAVANS and iRAVANS refer to exhalatory and inhalatory phases of respiratory-gated auricular vagal nerve stimulation, respectively. Non-statistically significant trends were found when analyzing the number of stimuli delivered (repeated-measures ANOVA F score = 2.58, p value = 0.07) and interstimulus intervals (F score = 2.67, p value = 0.06), suggesting slightly more stimuli and shorter ISI for iRAVANS on average. See Ref. [28] for additional details.

3.1. Causal influence of taVNS on BOLD fMRI activity

The causal medullary response to taVNS in both eRAVANS and iRAVANS (first analysis) is visualized in Fig. 5 (left and right, respectively). The eRAVANS →(BOLD Signal | Convolved HR) response map showed an elongated cluster (p value < 0.001) that extended rostroventrally within the rostromedial to rostrolateral medulla, consistent with the putative anatomical localization for the NTS ipsilateral to stimulation [58,59]. The same map demonstrated a small cluster located in the dorsal aspect of the rostral pons, consistent with LC, as well as a larger rostroventrally elongated cluster located within the olive, contralateral to stimulation. Interestingly, the iRAVANS →(BOLD Signal | Convolved HR) response map also showed two significant clusters (p value < 0.001), which in one case reproduced, albeit to a much lesser spatial extent, the cluster consistent with the NTS, as seen in the eRAVANS analysis. The other cluster was consistent with the anatomical location of the dorsomedial division of the periaqueductal gray (dmPAG) (see Fig. 6).

3.2. Cardiovagal modulation by brainstem regions

During eRAVANS, we found a causal influence of the BOLD fMRI signal in the PBN (ipsilateral to stimulation), nucleus reticularis parvocellularis (RtP), and pontine nuclei (PN) (contralateral to stimulation) on cardiovagal modulation as estimated through time-resolved HF-HRV. The causal influence of the BOLD fMRI signal in the RtP was also noted during iRAVANS, in addition to a causal influence of the BOLD fMRI signal in the ventrolateral PAG (vlPAG), contralateral to stimulation, on the HF-HRV time series.

4. Discussion

In this study, we combined ultrahigh field (7T) fMRI, time-resolved HF-HRV estimation based on point process modeling of the human heartbeat (i.e., a proxy for cardiovagal activity), and a recent reformulation of Granger causality to explore a) brainstem localization of the taVNS response and b) the brainstem (sub)network involved in relaying modulatory information to cardiovagal activity. The SS-GC approach generalizes the most commonly employed autoregressive model-based Granger causality (GC) to analytically handle autoregressive moving average processes (ARMA). This is a specific advantage for physiological signals, where a moving average component is often present. In particular, the SS-GC approach addresses the assumptions of linearity, stationarity and homoscedasticity, which are common in prior, more classical formulations of GC estimation, and guarantees robustness to downsampled, noisy and/or filtered data. This is particularly important when the signal, as in the case of the BOLD fMRI response to neuronal activity, is a downsampled and low-pass filtered version of the original (i.e., neural) effectors.

In the first part of the study, we reproduced and corroborated the results in Ref. [28] while demonstrating a possibly superior sensitivity and specificity of the SS-GC directed influence method compared to traditional, GLM-based analyses. Indeed, the differences between the results in Ref. [28] and the present findings are most likely to be attributed to our current statistical approach combined with fully nonparametric, permutation-based testing, which provides a robust method to eliminate potential confounds related to data acquisition and processing. These results lend further support to previous studies that have localized the human NTS response to taVNS afference while also highlighting previously unobserved fMRI responses in noradrenergic, autonomic regulation, and pain/homeostatic nuclei (e.g., LC, PAG).

In the second part of the study, we explored brainstem modulation of cardiovagal outflow (which our previous respiratory-gated taVNS studies have shown to be enhanced when stimuli occur during exhalation). We uncovered several nuclei that directly and causally influence cardiovagal outflow and are involved in parasympathetic efference, pain/homeostatic control and other visceral sensations (RtP, PAG, PBN).

Both the PBN and PAG are key brainstem nodes of the CAN. Located at the mesopontine level, the PBN acts as an interface between medullary reflex control and forebrain behavioral and integrative regulation of the ANS. The PBN receives gustatory, general visceral, and respiratory inputs from the NTS, as well as nociceptive and thermoreceptive inputs from the spinal cord, and conveys this information to the hypothalamus, amygdala, and thalamus [60]. It has been divided into thirteen distinct subnuclei and regions, each associated with a unique set of afferents, efferents, and neurotransmitters. Notably, invasive animal studies have implicated the PBN in cardiovascular regulation, with microstimulation studies reporting differential modulation of blood pressure and heart rate at various stimulation sites within the PBN. The specific cluster highlighted by our analysis appears to be consistent with the ventral portion of the medial PBN, putatively including the Kölliker-Fuse nucleus. Interestingly, the Kölliker-Fuse nucleus is known to directly participate in the control of respiration by modulating respiratory rate and pattern, specifically the transition from inhalation to exhalation [61]. The PAG connects the forebrain and brainstem autonomic control nuclei and includes four longitudinal columns parallel to the mesencephalic aqueduct, namely, the dorsomedial, dorsolateral, lateral, and ventrolateral PAG (vlPAG). This latter subregion receives extensive afferents from the NTS, and it is suggested to regulate passive defensive behaviors and opioid analgesia [60]. Stimulation of the vlPAG has been shown to evoke “passive coping” behaviors such as quiescence, hypotension, bradycardia, and opioid-mediated analgesia. Finally, the RtP is part of the ponto-medullary reticular formation, a complex structure of different cell types coordinating many reflexive and vital functions through its vast array of projections and networks [62,63]. The lateral tegmental field of the reticular formation, where the RtP is located, contains premotor neurons that project via long descending axons to spinal cord motor neurons, which participate in many autonomic functions, including respiration, regulation of abdominal pressure and function, micturition, and regulation of blood pressure. The causal link established here between PBN, vlPAG, and RtP activity and HF-HRV

Table 1
– Stimulation characteristics and individual ratings for the different conditions (mean ± SD; ISI: interstimulus interval).

Condition	# stimuli	ISI (s)	Current (mA)	Intensity (0–10 NRS)
eRAVANS	127.5 ± 22.0	2.9 ± 0.6	1.6 ± 2.3	4.5 ± 0.8
iRAVANS	136.1 ± 20.3	2.7 ± 0.5	1.7 ± 2.4	4.6 ± 0.8
Comparison statistic	F score = 2.58, p value = 0.07	F score = 2.67, p value = 0.06	F score = 0.45, p value = 0.64	F score = 0.06, p value = 0.56

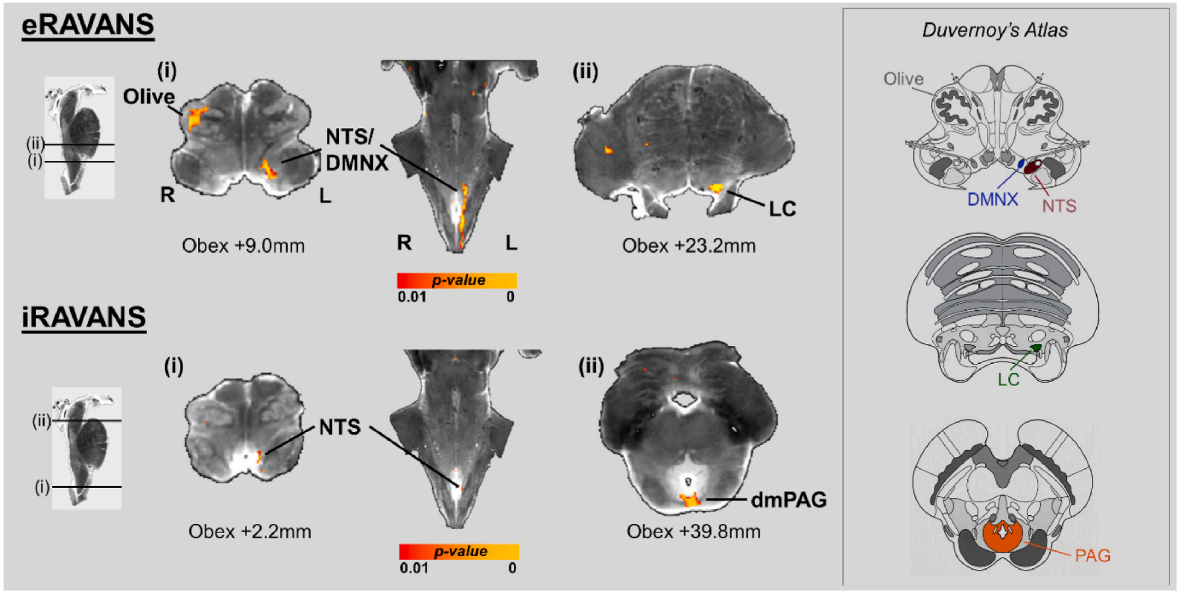

Fig. 5. – Group maps showing masked causal medullary responses to exhalatory taVNS (eRAVANS, top) and inhalatory taVNS (iRAVANS, bottom) overlaid on a high-resolution (0.2 mm) ex vivo brainstem. Group maps were derived by constructing the voxelwise null distribution for each specific hypothesis through within-subject permutation and comparing its medial to the median of the observed data distributions through statistical, nonparametric location testing cluster (p value $<$ 0.001). The eRAVANS clusters are consistent with putative NTS and LC (ipsilateral to stimulation) and olive (counterlateral to stimulation), while the iRAVANS clusters are again consistent with NTS ipsilateral with stimulation (albeit to a smaller spatial extent and with dmPAG.

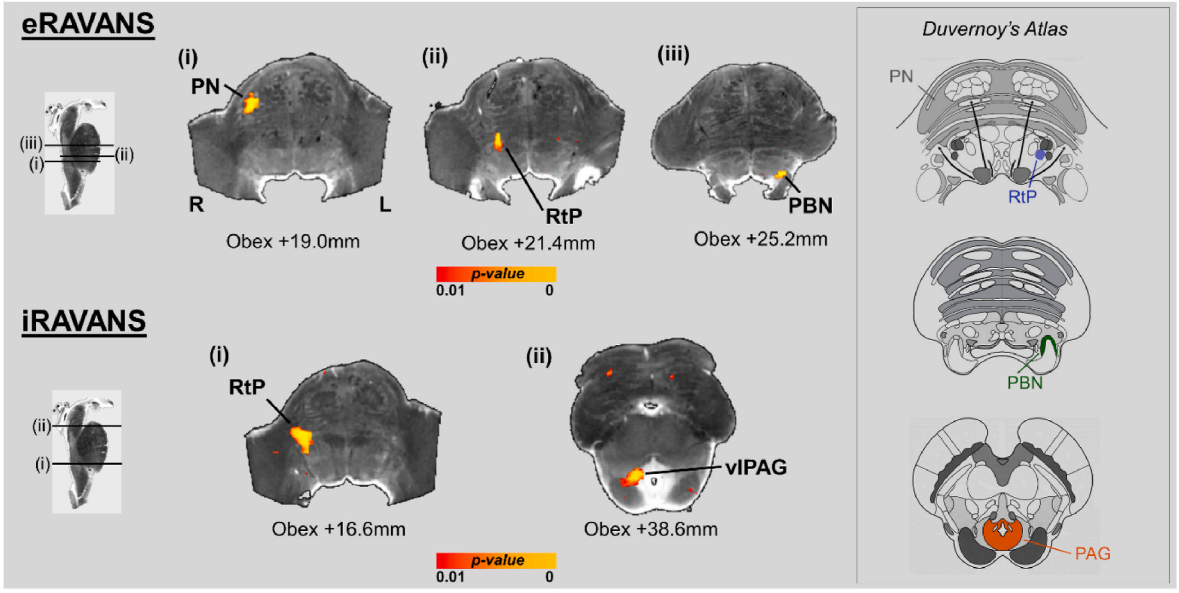

Fig. 6. – Group maps showing masked medullary regions that were seen to exert a causal influence on the time-resolved HF-HRV signal during exhalatory taVNS (eRAVANS, top) and inhalatory taVNS (iRAVANS, bottom) overlaid on a high-resolution (0.2 mm) ex vivo brainstem. For Fig. 5, group maps were derived by constructing the voxelwise null distribution for each specific hypothesis through within-subject permutation and comparing its median to the median of the observed data distributions through statistical, nonparametric location testing cluster (p value $<$ 0.001). The eRAVANS clusters are consistent with PBN (ipsilateral to stimulation) PN and RtP (counterlateral to stimulation), while the iRAVANS clusters are consistent with vlPAG and RtP (counterlateral to stimulation).

suggests a plausible brainstem mechanism to explain previously reported cardiovascular responses to taVNS.

Our study underscores the pivotal role of the vagus nerve in modulating physiological responses, particularly in the context of taVNS. The taVNS-evoked functional brainstem responses identified in our study, especially in the NTS, provide compelling evidence of the causal links between taVNS and fMRI response. Furthermore, our findings highlight the intricate interplay between various brainstem nuclei, including the NTS, locus coeruleus (LC), parabrachial nuclei (PBN), periaqueductal gray (PAG), and pontine raphe nuclei. These nuclei play a crucial role in cardiovascular control and are intricately involved in the cardiovagal response to taVNS. The enhanced sensitivity of our approach, compared to prior conventional methods, has allowed us to elucidate potential mechanisms by which information is relayed between these brainstem nuclei and the cardiovagal response. This deepened understanding provides valuable insight into the physiological mechanisms supporting efferent vagal responses, particularly in humans.

Our group-level analysis employed a null distribution generated by

permuting pairs of signals within our own dataset. This approach accounts for systemic confounds related to the data acquisition and processing pipeline and filters out a much larger share of unwanted variance compared to traditional parametric approaches, including variability that is not under explicit experimental control and/or cannot be controlled for by the use of statistical covariates. It should be noted that while an analytical statistic for testing the null hypothesis of zero GC exists (see, e.g., Ref. [64]), passing this first-level statistic up to the second level (e.g., for a classical mixed model analysis) would assume compliance with a number of additional assumptions commonly accepted for GLM analysis, related to, e.g., the parent distributions of the first-level statistics. More importantly, building the null distribution from experimental data by permuting under the null hypothesis allows (in addition to foregoing any assumptions of Gaussianity) accurate estimation of its shape on a voxelwise basis while effectively eliminating all possible experimental and algorithmic confounds related to the data acquisition and processing pipeline. While synthetic data-based studies would be necessary to substantiate this quantitatively, we speculate that the sensitivity is provided by the use of SS-GC to detect associations between time series, while the specificity is provided by the second level permutation-based analytical strategy.

Several limitations to our study should be noted. For instance, identification of putative brainstem autonomic nuclei is challenging due to their reduced size, lack of anatomical boundaries, and limited availability of atlases [11]. In an attempt to overcome these limitations, we visualized the results on a high-resolution brainstem volume and referred to several anatomical atlases to label the resulting clusters [58,59,65]. Furthermore, our original study also included an active control stimulation (earlobe, innervated by the greater auricular nerve and commonly used in taVNS studies as a sham), which also elicited a partly overlapping activation in the medulla, as well as an increase in HF-HRV [28]. While we presently focused on cymba conchae stimulation, which is known to be exclusively innervated by the auricular branch of the vagus nerve [66,67], future work should apply our proposed statistical framework to earlobe stimulation. Our approach could elucidate brainstem network specificity in controlling HRV upon vagal versus stimulation. Such an investigation may further contribute to understanding the mechanisms underlying cardiac and other effects of transcutaneous stimulation strategies, providing a more comprehensive view of the physiological implications of these interventions. Moreover, a limitation of our study is the small sample size, which may affect the generalizability of our findings. Future studies with larger cohorts are warranted to validate and expand upon our results. Finally, due to the low frequency at which BOLD fMRI signals are generated, in comparison to the dynamic scales of the neural activity – along with the limitations posed by the size of various brainstem nuclei in relation to the voxel size – Granger analysis may only have sufficient power to resolve the larger or more activate nuclei that are causally involved in response to taVNS stimulation. However, new Granger causality methods that are based on artificial neural networks (as described in Refs. [68,69]) in the future might prove more sensitive to possibly nonlinear taVNS-evoked interplay between brainstem nuclei, revealing more subtle activation patterns with greater sensitivity.

In conclusion, our causal approach allowed us to noninvasively evaluate directional interactions between fMRI BOLD signals and cardiovagal outflow, identifying relevant brainstem nuclei influencing heart rate variability response to taVNS. Moreover, our flexible framework can provide valuable insight into causal relations in numerous applications involving time series from a single modality or from multiple modalities.

CRediT authorship contribution statement

Nicola Toschi: Conceptualization, Methodology, Writing – original draft, Writing – review & editing. **Andrea Duggento:** Conceptualization, Methodology, Formal analysis, Data Curation, Writing – original draft, Writing – review & editing. **Riccardo Barbieri:** Methodology, Formal analysis, Writing – original draft, Writing – review & editing, Funding acquisition. **Ronald G. Garcia:** Methodology, Writing – original draft, Writing – review & editing. **Harrison P. Fisher:** Methodology, Data Curation, Writing – original draft, Writing – review & editing. **Norman W. Kettner:** Methodology, Writing – original draft, Writing – review & editing. **Vitaly Napadow:** Conceptualization, Writing – original draft, Writing – review & editing, Funding acquisition. **Roberta Sclocco:** Conceptualization, Methodology, Formal analysis, Data Curation, Writing – original draft, Writing – review & editing, Funding acquisition.

Declaration of competing interest

None.

Acknowledgments

We thank the following organizations for funding support: US National Institutes for Health (NIH), Office Of The Director (OT2-OD023867); Center for Functional Neuroimaging Technologies (P41-EB015896); National Institute of Mental Health (NIMH), NIH U54-MH118919; National Center for Complementary and Integrative Health (NCCIH), NIH (P01-AT009965, R21-AT011918, K01-AT012208); National Institute of Mental Health (NIMH), NIH (U54-MH118919); the Bernard Osher Foundation; and the American Heart Association (16GRNT26420084); Osher Center for Integrative Medicine (NIH NCCIH R21-AT011918, NIH NCCIH K01-AT012208)#NEXTGENERATIONEU (NGEU) and funded by the Italian Ministry of University and Research (MUR), National Recovery and Resilience Plan (NRRP), project MNESYS (PE0000006) (to NT)– A Multiscale integrated approach to the study of the nervous system in health and disease (DN. 1553 11.10.2022); by the MUR-PNRR M4C2I1.3 PE6 project PE00000019 Heal Italia (to NT); by the NATIONAL CENTRE FOR HPC, BIG DATA AND QUANTUM COMPUTING, within the spoke “Multiscale Modeling and Engineering Applications" (to NT); the EXPERIENCE project (European Union’s Horizon 2020 Research and Innovation Programme under grant agreement No. 101017727); the CROSSBRAIN project (European Union’s European Innovation Council under grant agreement No. 101070908). This work also involved the use of instrumentation supported by the NIH Shared Instrumentation Grant Program and/or High-End Instrumentation Grant Program; specifically, Grant no. S1-0RR023043.

References

[1] Herbert H, Moga MM, Saper CB. Connections of the parabrachial nucleus with the nucleus of the solitary tract and the medullary reticular formation in the rat. J Comp Neurol 1990;293(4):540–80.
[2] Karimnamazi H, Travers SP, Travers JB. Oral and gastric input to the parabrachial nucleus of the rat. Brain Res 2002;957(2):193–206.
[3] Herbert H, Saper CB. Organization of medullary adrenergic and noradrenergic projections to the periaqueductal gray matter in the rat. J Comp Neurol 1992;315(1):34–52.
[4] Loewy AD, Burton H. Nuclei of the solitary tract: efferent projections to the lower brain stem and spinal cord of the cat. J Comp Neurol 1978;181(2):421–49.
[5] Norgren R. Projections from the nucleus of the solitary tract in the rat. Neuroscience 1978;3(2):207–18.
[6] Van Bockstaele EJ, Peoples J, Telegan P. Efferent projections of the nucleus of the solitary tract to peri-locus coeruleus dendrites in rat brain: evidence for a monosynaptic pathway. J Comp Neurol 1999;412(3):410–28.
[7] Saper CB, Stornetta RL. Central autonomic system. In: The rat nervous system. fourth ed. Elsevier; 2015. p. 629–73.
[8] Garcia-Gomar MG, Strong C, Toschi N, Singh K, Rosen BR, Wald LL, et al. In vivo probabilistic structural atlas of the inferior and superior colliculi, medial and lateral geniculate nuclei and superior olivary complex in humans based on 7 Tesla MRI. Front Neurosci 2019;13:764.
[9] Bianciardi M, Strong C, Toschi N, Edlow BL, Fischl B, Brown EN, et al. A probabilistic template of human mesopontine tegmental nuclei from in vivo 7T MRI. Neuroimage 2018;170:222–30.
[10] Bianciardi M, Toschi N, Edlow BL, Eichner C, Setsompop K, Polimeni JR, et al. Toward an in vivo neuroimaging template of human brainstem nuclei of the

ascending arousal, autonomic, and motor systems. Brain Connect 2015;5(10):597–607.
[11] Sclocco R, Beissner F, Bianciardi M, Polimeni JR, Napadow V. Challenges and opportunities for brainstem neuroimaging with ultrahigh field MRI. Neuroimage 2018;168:412–26.
[12] Singh K, Garcia-Gomar MG, Cauzzo S, Staab JP, Indovina I, Bianciardi M. Structural connectivity of autonomic, pain, limbic, and sensory brainstem nuclei in living humans based on 7 Tesla and 3 Tesla MRI. Hum Brain Mapp 2022.
[13] Cauzzo S, Singh K, Stauder M, Garcia-Gomar MG, Vanello N, Passino C, et al. Functional connectome of brainstem nuclei involved in autonomic, limbic, pain and sensory processing in living humans from 7 Tesla resting state fMRI. Neuroimage 2022;250:118925.
[14] Singh K, Cauzzo S, Garcia-Gomar MG, Stauder M, Vanello N, Passino C, et al. Functional connectome of arousal and motor brainstem nuclei in living humans by 7 Tesla resting-state fMRI. Neuroimage 2022;249:118865.
[15] Kraus T, Hosl K, Kiess O, Schanze A, Kornhuber J, Forster C. BOLD fMRI deactivation of limbic and temporal brain structures and mood enhancing effect by transcutaneous vagus nerve stimulation. J Neural Transm 2007;114(11):1485–93.
[16] Dietrich S, Smith J, Scherzinger C, Hofmann-Preiss K, Freitag T, Eisenkolb A, et al. [A novel transcutaneous vagus nerve stimulation leads to brainstem and cerebral activations measured by functional MRI]. Biomed Tech 2008;53(3):104–11.
[17] Kraus T, Kiess O, Hosl K, Terekhin P, Kornhuber J, Forster C. CNS BOLD fMRI effects of sham-controlled transcutaneous electrical nerve stimulation in the left outer auditory canal - a pilot study. Brain Stimul 2013;6(5):798–804.
[18] Frangos E, Ellrich J, Komisaruk BR. Non-invasive access to the vagus nerve central projections via electrical stimulation of the external ear: fMRI evidence in humans. Brain Stimul 2015;8(3):624–36.
[19] Garcia RG, Lin RL, Lee J, Kim J, Barbieri R, Sclocco R, et al. Modulation of brainstem activity and connectivity by respiratory-gated auricular vagal afferent nerve stimulation in migraine patients. Pain 2017;158(8):1461–72.
[20] Yakunina N, Kim SS, Nam EC. Optimization of transcutaneous vagus nerve stimulation using functional MRI. Neuromodulation 2017;20(3):290–300.
[21] Badran BW, Mithoefer OJ, Summer CE, LaBate NT, Glusman CE, Badran AW, et al. Short trains of transcutaneous auricular vagus nerve stimulation (taVNS) have parameter-specific effects on heart rate. Brain Stimul 2018;11(4):699–708.
[22] Barbieri R, Matten EC, Alabi AA, Brown EN. A point-process model of human heartbeat intervals: new definitions of heart rate and heart rate variability. Am J Physiol Heart Circ Physiol 2005;288(1):H424–35.
[23] Napadow V, Dhond R, Conti G, Makris N, Brown EN, Barbieri R. Brain correlates of autonomic modulation: combining heart rate variability with fMRI. Neuroimage 2008;42(1):169–77.
[24] Valenza G, Sclocco R, Duggento A, Passamonti L, Napadow V, Barbieri R, et al. The central autonomic network at rest: uncovering functional MRI correlates of time-varying autonomic outflow. Neuroimage 2019;197:383–90.
[25] Tessa C, Toschi N, Orsolini S, Valenza G, Lucetti C, Barbieri R, et al. Central modulation of parasympathetic outflow is impaired in de novo Parkinson's disease patients. PLoS One 2019;14(1):e0210324.
[26] Napadow V, Edwards RR, Cahalan CM, Mensing G, Greenbaum S, Valovska A, et al. Evoked pain analgesia in chronic pelvic pain patients using respiratory-gated auricular vagal afferent nerve stimulation. Pain Med 2012;13(6):777–89.
[27] Sclocco R, Garcia RG, Kettner NW, Fisher HP, Isenburg K, Makarovsky M, et al. Stimulus frequency modulates brainstem response to respiratory-gated transcutaneous auricular vagus nerve stimulation. Brain Stimul 2020;13(4):970–8.
[28] Sclocco R, Garcia RG, Kettner NW, Isenburg K, Fisher HP, Hubbard CS, et al. The influence of respiration on brainstem and cardiovagal response to auricular vagus nerve stimulation: a multimodal ultrahigh-field (7T) fMRI study. Brain Stimul 2019;12(4):911–21.
[29] Badran BW, Dowdle LT, Mithoefer OJ, LaBate NT, Coatsworth J, Brown JC, et al. Neurophysiologic effects of transcutaneous auricular vagus nerve stimulation (taVNS) via electrical stimulation of the tragus: a concurrent taVNS/fMRI study and review. Brain Stimul 2018;11(3):492–500.
[30] Miyazaki M, Arata A, Tanaka I, Ezure K. Activity of rat pump neurons is modulated with central respiratory rhythm. Neurosci Lett 1998;249(1):61–4.
[31] Miyazaki M, Tanaka I, Ezure K. Excitatory and inhibitory synaptic inputs shape the discharge pattern of pump neurons of the nucleus tractus solitarii in the rat. Exp Brain Res 1999;129(2):191–200.
[32] Baekey DM, Molkov YI, Paton JF, Rybak IA, Dick TE. Effect of baroreceptor stimulation on the respiratory pattern: insights into respiratory–sympathetic interactions. Respir Physiol Neurobiol 2010;174(1–2):135–45.
[33] Polimeni JR, Bhat H, Witzel T, Benner T, Feiweier T, Inati SJ, et al. Reducing sensitivity losses due to respiration and motion in accelerated echo planar imaging by reordering the autocalibration data acquisition. Magn Reson Med 2016;75(2):665–79.
[34] Jenkinson M, Beckmann CF, Behrens TE, Woolrich MW, Smith SM. Fsl. Neuroimage 2012;62(2):782–90.
[35] Cox RW. AFNI: software for analysis and visualization of functional magnetic resonance neuroimages. Comput Biomedl Res Int J 1996;29(3):162–73.
[36] Fonov V, Evans AC, Botteron K, Almli CR, McKinstry RC, Collins DL, et al. Unbiased average age-appropriate atlases for pediatric studies. Neuroimage 2011;54(1):313–27.
[37] Calabrese E, Hickey P, Hulette C, Zhang J, Parente B, Lad SP, et al. Postmortem diffusion MRI of the human brainstem and thalamus for deep brain stimulator electrode localization. Hum Brain Mapp 2015;36(8):3167–78.
[38] Avants BB, Tustison NJ, Stauffer M, Song G, Wu B, Gee JC. The Insight ToolKit image registration framework. Front Neuroinf 2014;8:44.
[39] Napadow V, Dhond R, Kennedy D, Hui KK, Makris N. Automated brainstem co-registration (ABC) for MRI. Neuroimage 2006;32(3):1113–9.
[40] Force T. Heart rate variability: standards of measurement, physiological interpretation and clinical use. Task Force of the European Society of Cardiology and the North American Society of Pacing and Electrophysiology. Circulation 1996;93(5):1043–65.
[41] Sclocco R, Kim J, Garcia RG, Sheehan JD, Beissner F, Bianchi AM, et al. Brain circuitry supporting multi-organ autonomic outflow in response to nausea. Cerebr Cortex 2016;26(2):485–97.
[42] Sclocco R, Beissner F, Desbordes G, Polimeni JR, Wald LL, Kettner NW, et al. Neuroimaging brainstem circuitry supporting cardiovagal response to pain: a combined heart rate variability/ultrahigh-field (7 T) functional magnetic resonance imaging study. Philosoph Transact Series A, Math, Phys Eng Sci 2016;374(2067).
[43] Lindquist MA, Meng Loh J, Atlas LY, Wager TD. Modeling the hemodynamic response function in fMRI: efficiency, bias and mis-modeling. Neuroimage 2009;45(1 Suppl):S187–98.
[44] Barnett L, Seth AK. Granger causality for state-space models. Phys Rev E - Stat Nonlinear Soft Matter Phys 2015;91(4):040101.
[45] Granger CWJ. Investigating causal relations by econometric models and cross-spectral methods. Econometrica 1969;37(3):424–38.
[46] Stephan KE, Roebroeck A. A short history of causal modeling of fMRI data. Neuroimage 2012;62(2):856–63.
[47] Valdes-Sosa PA, Roebroeck A, Daunizeau J, Friston K. Effective connectivity: influence, causality and biophysical modeling. Neuroimage 2011;58(2):339–61.
[48] Friston K, Moran R, Seth AK. Analysing connectivity with Granger causality and dynamic causal modelling. Curr Opin Neurobiol 2013;23(2):172–8.
[49] Seth AK, Chorley P, Barnett LC. Granger causality analysis of fMRI BOLD signals is invariant to hemodynamic convolution but not downsampling. Neuroimage 2013;65:540–55.
[50] Duggento A, Passamonti L, Valenza G, Barbieri R, Guerrisi M, Toschi N. Multivariate Granger causality unveils directed parietal to prefrontal cortex connectivity during task-free MRI. Sci Rep 2018;8(1):5571.
[51] Friston KJ, Mechelli A, Turner R, Price CJ. Nonlinear responses in fMRI: the Balloon model, Volterra kernels, and other hemodynamics. Neuroimage 2000;12(4):466–77.
[52] Izhikevich EM, Gally JA, Edelman GM. Spike-timing dynamics of neuronal groups. Cerebr Cortex 2004;14(8):933–44.
[53] Izhikevich EM. Simple model of spiking neurons. IEEE Trans Neural Network 2003;14(6):1569–72.
[54] Mill RD, Bagic A, Bostan A, Schneider W, Cole MW. Empirical validation of directed functional connectivity. Neuroimage 2017;146:275–87.
[55] Rodrigues J, Andrade A. Lag-based effective connectivity applied to fMRI: a simulation study highlighting dependence on experimental parameters and formulation. Neuroimage 2014;89:358–77.
[56] Fernandes TT, Direito B, Sayal A, Pereira J, Andrade A, Castelo-Branco M. The boundaries of state-space Granger causality analysis applied to BOLD simulated data: a comparative modelling and simulation approach. J Neurosci Methods 2020;341:108758.
[57] Chang C, Cunningham JP, Glover GH. Influence of heart rate on the BOLD signal: the cardiac response function. Neuroimage 2009;44(3):857–69.
[58] Naidich TP, Duvernoy HM, Delman BN, Sorensen AG, Kollias SS, Haacke EM. Duvernoy's atlas of the human brain stem and cerebellum. Vienna: Springer Vienna; 2009.
[59] Olszewski J, Baxter D. Cytoarchitecture of the human brain stem. Cytoarchitecture of the human brain stem. 1954.
[60] Benarroch EE. Central autonomic control. Primer on the autonomic nervous system. third ed. Elsevier; 2012. p. 9–12.
[61] Varga AG, Maletz SN, Bateman JT, Reid BT, Levitt ES. Neurochemistry of the Kolliker-Fuse nucleus from a respiratory perspective. J Neurochem 2021;156(1):16–37.
[62] Horn AK. The reticular formation. Prog Brain Res 2006;151:127–55.
[63] Wang D. Reticular formation and spinal cord injury. Spinal Cord 2009;47(3):204–12.
[64] Geweke J. Measurement of linear dependence and feedback between multiple time series. J Am Stat Assoc 1982;77(378):304–13.
[65] Paxinos G, Huang X-F. Atlas of the human brainstem. Elsevier; 2013.
[66] Peuker ET, Filler TJ. The nerve supply of the human auricle. Clin Anat 2002;15(1):35–7.
[67] Neuhuber WL, Berthoud H-R. Functional anatomy of the vagus system–Emphasis on the somato-visceral interface. Auton Neurosci 2021;236:102887.
[68] Duggento A, Guerrisi M, Toschi N. Echo state network models for nonlinear Granger causality. Philosoph Transact Series A, Math, Phys Eng Sci 2021;379(2212):20200256.
[69] Tank A, Covert I, Foti N, Shojaie A, Fox EB. Neural granger causality. IEEE Trans Pattern Anal Mach Intell 2022;44(8):4267–79.